

Physics-based 0D-U-I-SoC cell performance model for aqueous organic redox flow batteries

Gael Mourouga^{a,1,*}, Roman P. Schaerer^{1,a}, Xian Yang^b, Tobias Janoschka^b, Thomas J. Schmidt^{c,d}, Juergen O. Schumacher^a

^a Institute of Computational Physics, ZHAW, Wildbachstr. 21, Winterthur CH-8400, Switzerland

^b JenaBatteries GmbH, Otto-Schott-Strasse 15, Jena 07745, Germany

^c Paul Scherrer Institut, Electrochemical Laboratory, Forschungsstrasse 111, Villigen PSI CH-5232, Switzerland

^d ETH Zurich, Laboratory for Physical Chemistry, CH Zurich 8092, Switzerland

ARTICLE INFO

Keywords:

AORFB
All-organic chemical system
Performance prediction
Sensitivity analysis
Open-source software

ABSTRACT

Aqueous organic redox-flow batteries are an emerging technological solution in the field of grid-scale energy storage, owing to their long lifetime, safety, chemical flexibility, potential for low cost and environmental friendliness. In this work we present a physics-based dimensionality reduced model for the performance prediction of aqueous organic redox flow batteries. The model allows for fast evaluations of the cell voltage and power density, which are expressed explicitly in terms of the electric current density and state of charge. The model takes into consideration important phenomena, such as the activation and concentration overpotentials in the electrodes as well as the non-negligible electro-osmotic drag of water through the membrane. A sensitivity analysis of the model indicates the influence of various model parameters at different current densities on the predicted cell voltage. In this work we found the formal potentials and ohmic cell resistance to be the most critical parameters for performance prediction. Experimental parameterization and validation on cycling and polarization experiments revealed good agreement with the experiments within a predicted range of validity due to the different simplifying assumptions.

1. Introduction

The rise of intermittent energy generation sources in the last decade has increased the need for peak shifting and frequency regulation on the European grid, resulting in a push for research and development in grid-scale energy storage technologies. Redox-flow batteries (RFB) are a promising emerging technology for this application as they allow for an independent scaling of energy capacity and power enabling a flexible adaptation to the local energy grid requirements, see e.g. [1]. In particular, aqueous organic redox flow batteries (AORFB) have attracted increasing interest from researchers and industry, owing to their long lifetime, low electrolyte cost, safety (non-flammability) and lower supply-chain risks compared to metal-based materials [2,3].

Modelling physico-chemical processes within a battery is important as it allows optimizing the battery operating parameters, the electrolyte formulations, or battery components such as the flow frame and the membrane. However, developing accurate models involves an interplay

between a plethora of different scientific disciplines and typically relies on mathematical description of more than one physical phenomenon at the same time. A wide variety of approaches can therefore be favored, depending on the aim of the required accuracy and predictive power of the model, as well as the number of input parameters and validation experiments available. Most cell-scale models can be broadly categorized according to three approaches: Equivalent-Circuit (EC) models, lumped continuum models and spatially-resolved models.

Equivalent circuit models [4,5] typically describe the battery system as a sum of components (resistances, capacitance, inductance) with varying levels of complexity, which are typically fitted to experimental measurements, yielding e.g. current-voltage-temperature relationships. These models are relatively simple to design and fast to compute, but may lack in accuracy and/or predictive power upon changing components of the battery. They are often favored in field control applications at the stack level [6].

Spatially-resolved models range from simplified 1D [7] to fully 3D

* Corresponding author.

E-mail address: gaelmourouga@protonmail.com (G. Mourouga).

¹ Both authors contributed equally to this work.

resolved models [8–11]. These models provide more insight into the physical processes occurring in a redox-flow battery, and make up the majority of the literature on cell-scale modelling [12]. Possible issues with these models include their high computational cost and the large number of ex-situ input parameters required to reach better predictive power than EC models. Also, the impact of simplifying assumptions, such as the dilute solution hypothesis is rarely quantified, but a growing number of authors [13,14] advocate for more rigorous modelling of the thermodynamics of concentrated aqueous solutions reacting in flow batteries.

Finally, lumped physics-based continuum models, as presented in [15,16], neglect spatial variations of the electrolyte flow and composition within the electrodes. As shown by [15] this is a valid approximation within a certain window of operation, allowing for a dimensional reduction of the model to 0D. These models allow simulating (averaged) cell voltage for as wide range of conditions [15,16], enabling cell lifetime studies [17], investigations on oxygen and hydrogen reduction at the electrodes [18] and more importantly allow for extensive parameter studies, sensitivity analyses and thermodynamic modelling thanks to their reduced computational cost [19].

In this paper, we present a novel physics-based single-cell model for aqueous organic redox flow batteries (referred to as 0D-U-I-SoC model in the following). The model allows evaluating the cell voltage and power density as steady-state solutions in terms of the applied operating conditions. As such, the 0D-U-I-SoC model provides predictions of the cell performance over time spans much shorter than the characteristic time scales of non-negligible irreversible processes, such as cross-over of electro-active species. The simplifying model assumptions allow establishing a one-to-one mapping between the SoC and electrolyte composition. Furthermore, an explicit mapping from the current operating conditions, such as the SoC and the electric current density to the cell voltage can be derived, allowing for a run time on the order of only 1ms for a single voltage evaluation. Thus, the 0D-U-I-SoC model enables rapid explorations of the cell performance landscape in terms of critical cell parameters, such as the ohmic cell resistance, the mass transfer coefficient or the volumetric flow rate.

The model is applied to an all-organic aqueous electrolyte system first introduced in 2016 [1] and described in more details in Section 3.

In contrast to dimensionality-reduced models available in the literature [15,16,18], the present model considers also the electro-osmotic drag of water through the membrane, as well as density changes during the charge-discharge cycling, which cause SoC-dependent changes of the electrolyte volume. Furthermore, a sensitivity analysis of the model shows the impact of the operating conditions on the cell

performance and allows for a ranking of the model parameters in terms of sensitivity.

The presented model aims at being a building block towards fully physics-based models with a minimum amount of fitted parameters and is implemented in Mathematica, published as open-source software under a 3-clause BSD license allowing for full code inspection and reuse of the model in other works.

After stating the geometry and assumptions of the model based on the experimental setup, a one-to-one mapping between the SoC and composition is given in Section 4, which accounts for density changes and the electro-osmotic drag effect. An explicit expression of the cell voltage is derived as a function of the state of charge and the current density in Section 5. The validity range of the model is discussed in Section 6 and results and experimental validation are shown in Section 7.

2. Model geometry and simplifying assumptions

We consider the simplified cell geometry of a flow battery shown in Fig. 1, which is composed of a negative and a positive electrode compartments, separated by a membrane. The electrode compartments are fitted with porous electrode material through which electrolyte flows by forced convection.

We are interested in predicting the overall cell voltage and power density in terms of the applied electric current and state of charge of the battery for a range of typical operating conditions over time scales that are much shorter than diffusive and osmotic fluxes through the membrane and irreversible degradation processes of the electrolyte material or cell components. Furthermore, we assume the electric current density to be small enough for spatial concentration variations of the electro-active species to be negligible in the electrode compartments. The operating conditions and cell properties are assumed to generate negligible spatial and temporal temperature variations allowing the usage of an isothermal model.

Clearly, these assumptions are only satisfied within a specific range of operating conditions and observation time scales. We discuss the impact of the above assumptions on the model validity range in Section 6.

3. Experimental section

3.1. Electrolytes

Experiments were carried out on the aqueous organic TEMPTMA (N,

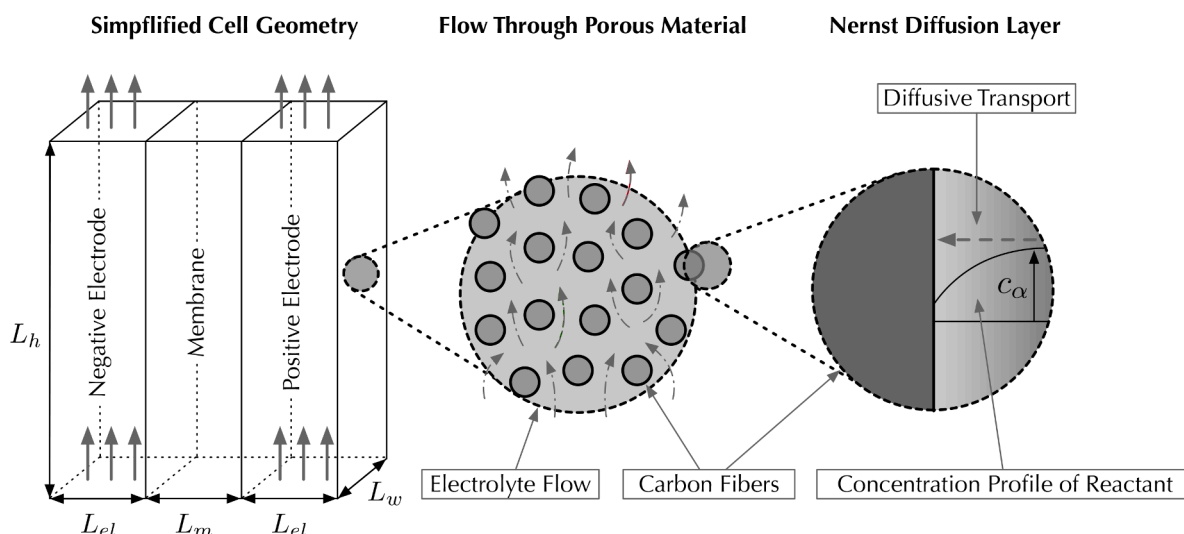
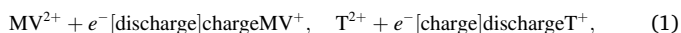


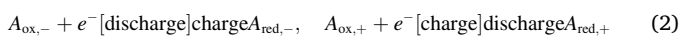
Fig. 1. Illustration of simplified cell geometry and transport through porous electrode and Nernst layer.

N,N-2,2,6,6-heptamethylpiperidinyloxy-4-ammonium chloride) / Methyl Viologen (*N,N*A'-dimethyl-4,4'-bipyridinium dichloride) system, first introduced in 2016 [1]. Electrolytes were used as received, and only diluted in deionized water to reach the desired concentrations.

Figure 2 shows a graphical representation of the half-cell redox reaction of the chemical system. The electrochemical half-cell reactions in the negative and positive half-cells are given by



where T denotes the TEMPTMA species and MV is the Methyl Viologen species. To allow for a more succinct notation we write the half-cell reactions (1) in the following as



with the corresponding stoichiometric coefficients given by $\nu_{\text{ox},\pm} = -1$, $\nu_{\text{red},\pm} = 1$, where the subscripts $\{-, +\}$ refer to the negative and positive half-cell, respectively.

3.2. Test cells

Test cells with an active surface area of 5cm^2 and flow fields in flow-through configuration were provided by JenaBatteries GmbH. Two GFD 4.6 EA carbon felt electrodes from SGL Carbon were sandwiched around a Fumasep FAA-3-50 anion-exchange membrane, immersed for at least 24h in a 0.5M NaCl solution to ensure both proper wetting (swelling) and the presence of chloride counter-ions in the membrane phase. Relevant dimensions are presented in Table 1. These comparatively small test cells were chosen to minimize the amount of electrolyte and ion-exchange membrane material required in the experiments.

3.3. Charge/discharge experiments

In a typical charge/discharge experiment, reservoirs of volume $V = 10\text{ mL}$ were connected to the test cells with Tygon S3 L-EFL 1.6 mm \times 4.8 mm tubing passing through a Heidolph Pumpdrive 5201, MASTERFLEX peristaltic pump. After a few minutes of electrolyte circulation, the cell resistance was measured through Electrochemical Impedance Spectroscopy (EIS), and the cell was charged/discharged once at a low electric current density of $\pm 20\text{ mA cm}^{-2}$ to assess a correct depth-of-discharge. We used cut-off voltage values of 1.5 V and 0.9 V, to ensure the absence of water electrolysis while maximizing the practical state of charge (SoC) window. Relevant operational parameters to the rest of the cycling protocol are shown in Table 1.

3.4. Solvent transfer experiment

To measure the solvent transfer during one cycle, a single charge was performed and the carbon felt electrodes, tubes and reservoirs (composition indicated in Table 1) were weighed before and after the experiment. In order to have a better control over the flow rate and avoid important pressure gradients, the peristaltic pumps were replaced with SIMDOS 10 diaphragm liquid dosing pumps.

The mass of chloride ions transferred between the reservoirs during

charge was calculated according to the charging time, the charging current and the molar mass of chloride ions, and the remaining mass was attributed to water, assuming a perfectly perm-selective membrane, which allowed to calculate the experimental electro-osmotic coefficient of chloride ions.

3.5. Polarisation experiments

In a typical polarisation experiment, the cell was first charged to the desired SoC at constant current density of 20 mA cm^{-2} , then discharged for 30 s at the desired current density. The average value of the obtained voltage was reported on the polarisation plots (Fig. 9 in Section 7) showing cell voltage as a function of current density.

In a second experiment, we attempted to limit several sources of experimental uncertainties: we used bigger reservoirs (100 mL) placed in 1 L water baths to limit both uncertainties on the SoC due to fast charging and on the cell temperature due to Joule heating at high currents, and the peristaltic pumps were replaced with SIMDOS 10 diaphragm liquid dosing pumps to limit uncertainties on the flow rate. Results are presented for SoC 20 on Fig. 9b.

3.6. Experimental parameters

4. Relationship between state of charge and composition

The state of charge (SoC) of a battery is a function of the available capacity Q given by

Table 1
Operating conditions for different experiments.

Parameter Description	Symbol	Value
Cell geometry		
Electrode thickness (through-plane direction)	L_{el}	0.4 cm
Electrode width (in-plane)	L_w	2.236 cm
Electrode height (in-plane)	L_h	2.236 cm
Membrane thickness (dry)	L_m	50 μm
Membrane thickness (wet)	L_m	80 μm
General		
Room temperature	T	298.15 K
Cut-off voltage (high)	U_h	1.5 V
Cut-off voltage (low)	U_l	0.9 V
Initial molar concentration of $\text{MV}^{2+}\text{Cl}_2^-$	$c_{\text{ox},-}$	1.49 mol L^{-1}
Initial molar concentration of T^+Cl^-	$c_{\text{red},+}$	1.12 mol L^{-1}
Electrolyte flow rate	\dot{V}	16 ml/min
Charge/discharge experiment		
Electrolyte volume	V	10 mL
Current	I	400 mA
Solvent transfer experiment		
Electrolyte volume	V	50 mL
Current	I	100 mA
Polarisation experiment		
Electrolyte volume	V	100 mL
Supporting water bath volume	L_T	1 L

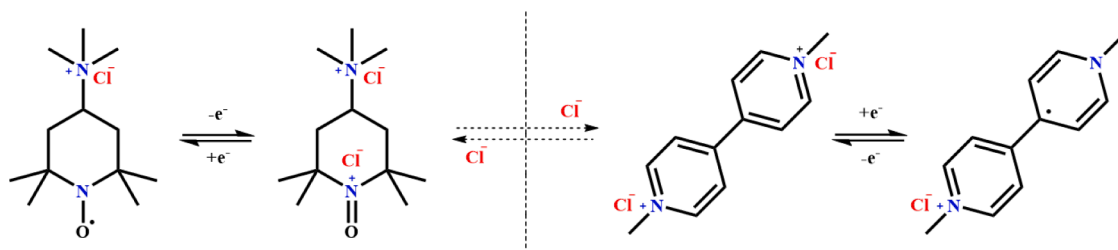


Fig. 2. Reduced and oxidized forms of TEMPTMA (left) and Methyl Viologen (right) salts in chloride form.

$$\text{SoC}(Q) = \frac{Q}{Q_{\max}}, \quad (3)$$

where Q_{\max} denotes the theoretical maximal capacity. For the one-electron electrochemical reactions considered here, the maximum amount of substance being consumed or produced is related to the maximum capacity by

$$\Delta n_{\max} = \frac{Q_{\max}}{F}, \quad (4)$$

where F denotes Faraday's constant. The amount of substances of the reduced and oxidized species in the negolyte and posolyte can be expressed in terms of the state of charge as

$$\begin{aligned} n_{\text{red},-}(\text{SoC}) &= \text{SoC} \cdot \Delta n_{\max}, \\ n_{\text{ox},-}(\text{SoC}) &= n_{\text{ox},-}(0) - \text{SoC} \cdot \Delta n_{\max}, \\ n_{\text{red},+}(\text{SoC}) &= n_{\text{red},+}(0) - \text{SoC} \cdot \Delta n_{\max}, \\ n_{\text{ox},+}(\text{SoC}) &= \text{SoC} \cdot \Delta n_{\max}. \end{aligned} \quad (5)$$

In this study, the initial amount of electroactive species $n_{\text{ox},-}(0)$ and $n_{\text{red},+}(0)$ satisfy $n_{\text{ox},-}(0) > n_{\text{red},+}(0)$, so that $\Delta n_{\max} = n_{\text{red},+}$ and the maximum capacity is limited by the amount of the reduced species in the posolyte

$$Q_{\max} = F n_{\text{red},+}. \quad (6)$$

The amount of electroactive substances are thus linearly depending on the SoC as shown in Fig. 4. This does not, however, imply a linear dependence of the molar concentrations on the SoC as shown in the same figure, due to a variety of effects leading to volumetric changes, such as osmosis and electro-osmotic flow across the membrane or changes in the partial molar volumes.

4.1. Bulk concentrations in electrodes

Due to the consumption or production of electroactive species within the electrode compartments, the species bulk concentrations vary between the inflow and outflow boundaries. Since the membrane is assumed to be perfectly impermeable to the electroactive species, the conservation of mass allows to express the outflow species concentration in terms of the inflow concentration and the electric current as

$$c_{\alpha,\pm}^{\text{out}} = c_{\alpha,\pm}^{\text{in}} \mp \frac{\nu_{\alpha} I}{F \dot{V}}, \quad (7)$$

where \dot{V} denotes the volumetric mass flow rate. In the current model, the species bulk concentration, $c_{\alpha,\pm}^b$, is approximated by the arithmetic average between the inflow and outflow concentrations

$$c_{\alpha,\pm}^b \equiv c_{\alpha,\pm}^{\text{avg}} = c_{\alpha,\pm}^{\text{in}} \mp \frac{\nu_{\alpha} I}{2F \dot{V}}. \quad (8)$$

For the model to be physically sound we require that the electrolyte concentrations remain non-negative throughout the porous electrode. As shown in Appendix G this requirement is fulfilled for the system parameters studied in this paper.

Table 2
Molar masses of the electrolyte species.

Parameter Description	Symbol	Value
Molar mass of water	$M_{\text{H}_2\text{O}}$	18.02 g mol ⁻¹
Molar mass of chloride	M_{Cl^-}	35.45 g mol ⁻¹
Molar mass of TEMPTMA-Chloride	M_{TCl}	249.8 g mol ⁻¹
Molar mass of Methyl Viologen-Dichloride	M_{MVCl_2}	257.16 g mol ⁻¹

4.2. Density changes due to chemical reactions

Differences in the molar mass, see Table 2, and solvation shell of the charged and discharged forms lead to macroscopic variations in the density of electrolytes in the battery.

Figure 3 shows experimentally determined mass densities for the binary TEMPTMA and Methyl Viologen electrolyte solutions in terms of the molar concentration, together with linear least-square model approximations. For the discharged forms only the mass density of pure water and a single experimental value, at a higher molar concentration than shown in the plot, are used to define the linear model fit. This approximation is justified by the very linear behaviour of the mass density of uncharged aqueous solutions in this concentration range.

4.3. Water transfer

The transport of charged particles through the membrane is accompanied by the transfer of solvent molecules in the solvation shell of the exchanged ions. The electro-osmotic drag coefficient κ_s refers to the number of transported solvent molecules per chloride ion, which is related to the size of their solvation shell $\xi_{\text{Cl}^-} = 6$, see e.g. [20]. The amount of solvent molecules in moles, denoted by $n_{0,\pm}$ in the posolyte and negolyte respectively, can then be expressed in terms of the state of charge as

$$n_{0,\pm}(\text{SoC}) = n_{0,\pm}(0) \pm \kappa_s \cdot \Delta n_{\max} \cdot \text{SoC}. \quad (9)$$

To verify this value experimentally, a 50 mL 1.12M TEMPTMA / 1.49M MV cell was charged at 20 mA cm⁻² for 20 h and 33 min. The carbon felt electrodes, tubing and reservoirs were weighed before and after charging, and the experiment was repeated twice.

The posolyte side, gained [7.54, 7.94]g, while the negolyte side lost [8.04, 9.15]g. The small discrepancy can be explained by a net mass loss between cell disassembling and weighing, due to evaporation or droplets spattering. Using the molar masses in Table 2, this can be converted to 2.72 g of chloride ions and, consequently, [5.37, 5.71] g of water transferred between the reservoirs during cycling.

These results indicate that on average [3.83, 4.19] water molecules per chloride ions are carried across the membrane, which is below the expected size of the hydration shell of chloride ions. The experimental discrepancy can be explained by an imperfectly permselective membrane and/or a small influence of osmosis over the timescale of the experiment. As demonstrated in Section 8, the electro-osmotic coefficient has a relatively minor impact on the model, and to remain consistent with the model hypothesis we approximated the electro-osmotic coefficient with its theoretical value $\kappa_s = \xi_{\text{Cl}^-} = 6$. In Fig. 5 the resulting change of the total electrolyte volume in the negative and positive compartments is shown as a function of SoC.

5. Cell voltage model

The cell voltage model we consider in this work is inspired by the works of Heintz and Illenberger [21], Pavelka et al. [13], Murthy et al. [16] and del Olmo et al. [22]. It is not spatially-resolved, as we make the hypothesis that concentration can be assumed constant between electrode inlet and outlet (and by extension, in the reservoirs, a hypothesis which is discussed in Section 6).

As such, the cell voltage can be expressed as

$$U_{\text{cell}} = U_{\text{OCV}} + U_{\text{ohmic}} + \eta_{\text{tot}}, \quad (10)$$

where U_{OCV} denotes the open-circuit voltage, U_{ohmic} is the overall ohmic term due to the electric resistance of the cell, and $\eta_{\text{tot}} = \eta_{\text{act}} + \eta_{\text{conc}}$ is the total overpotential including the activation and mass transfer overpotentials.

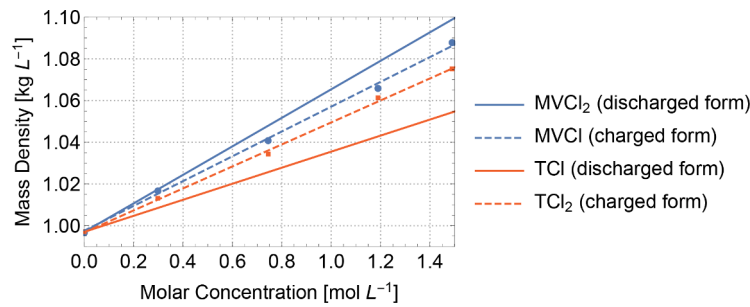


Fig. 3. Mass density measurements of binary electrolyte solutions, together with a linear fit.

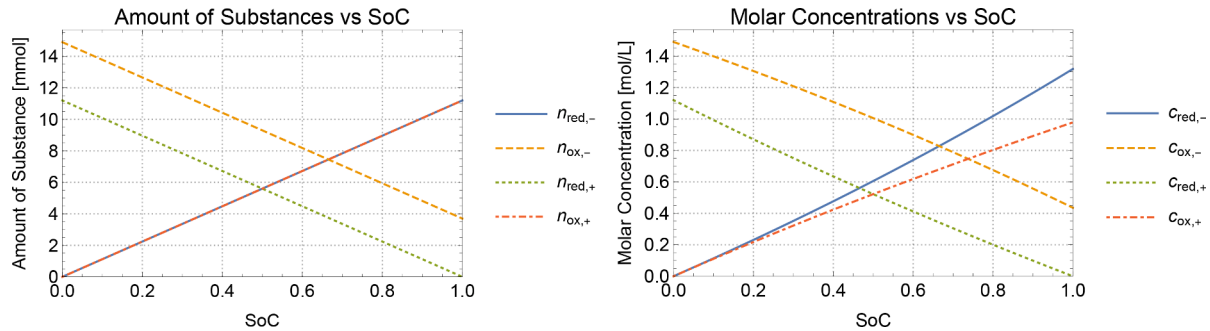


Fig. 4. Amount of substance and molar concentration as a function of state of charge.

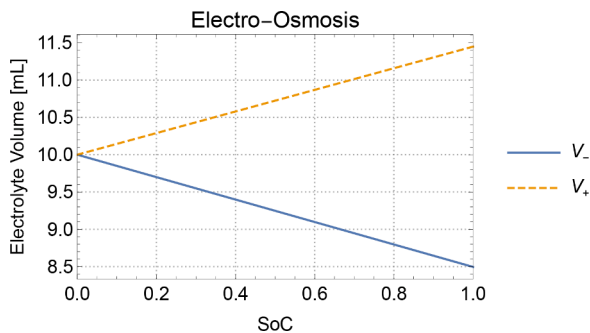


Fig. 5. Total electrolyte volume as a function of state of charge.

5.1. Open-circuit voltage

The open circuit cell voltage is determined by

$$U_{OCV} = U_{eq,+} - U_{eq,-} + U_{eq,m}, \quad (11)$$

where $U_{eq,+}$ and $U_{eq,-}$ denote the reversible half-cell potentials of the positive and negative half-cell, respectively, and $U_{eq,m}$ is the membrane potential that results from a gradient of concentration of ionic species across the membrane.

The half-cell potentials can be expressed in terms of the bulk concentrations $c_{\alpha,\pm}^b$ by the Nernst relation

$$U_{eq,\pm} = U_{eq,\pm}^{\circ} + U'_{eq,\pm} \quad (12)$$

with

$$U'_{eq,\pm} = U_{eq,\pm}^{\circ} - \frac{RT}{F} \ln \left(\frac{\gamma_{red,\pm}^b}{\gamma_{ox,\pm}^b} \right), \quad U'_{eq,\pm} = -\frac{RT}{F} \ln \left(\frac{c_{red,\pm}^b}{c_{ox,\pm}^b} \right), \quad (13)$$

where $U_{eq,\pm}^{\circ}$ and $U_{eq,\pm}^{\circ}$ denote the reference thermodynamic potential and the formal potential, respectively, see e.g. [23] or [24]. The bulk

(molar) activity coefficient $\gamma_{\alpha,\pm}^b$ of species α is related to the bulk activity coefficient $a_{\alpha,\pm}^b$ by $a_{\alpha,\pm}^b = c_{\alpha,\pm}^b \gamma_{\alpha,\pm}^b / c^{\circ}$, where c° denotes a reference molar concentration at which the electrolytes are assumed to follow an ideal behavior, usually taken as $c^{\circ} = 1 \text{ mol L}^{-1}$ for convenience.

As shown in Appendix C, the membrane potential is given by

$$U_{eq,m} = U'_{eq,m} + U'_{eq,m} \quad (14)$$

with

$$U'_{eq,m} = \frac{RT}{F} \ln \left(\frac{\gamma_{Cl,-}^b}{\gamma_{Cl,+}^b} \right) \quad \text{and} \quad U'_{eq,m} = \frac{RT}{F} \ln \left(\frac{c_{red,+}^b + 2c_{ox,+}^b}{c_{red,-}^b + 2c_{ox,-}^b} \right). \quad (15)$$

Collecting the formal potentials allows to rewrite the open circuit potential as

$$U_{OCV} = U'_{eq,+} + (U'_{eq,+} - U'_{eq,-}) + U'_{eq,m}, \quad (16)$$

where $(U'_{eq,+} - U'_{eq,-})$ can be written in terms of the stoichiometric reaction quotient of the overall cell (discharging) reaction as

$$(U'_{eq,+} - U'_{eq,-}) = -\frac{RT}{F} \ln(Q_R), \quad \text{with} \quad Q_R = \frac{c_{red,+}^b c_{ox,-}^b}{c_{ox,+}^b c_{red,-}^b}, \quad (17)$$

where Q_R denotes the reaction quotient of the overall cell reaction and the total formal potential U_{eq}° can be expressed in terms of measurable mean activity coefficients

$$\gamma_{red,\pm}^{b,\pm} = \sqrt{\gamma_{red,\pm}^b \gamma_{Cl,\pm}^b}, \quad \gamma_{ox,\pm}^{b,\pm} = \sqrt[3]{\gamma_{ox,\pm}^b (\gamma_{Cl,\pm}^b)^2}, \quad (18)$$

yielding

$$U_{eq}^{\circ} = \frac{RT}{F} \ln \left(\frac{(\gamma_{red,+}^{b,\pm})^2 (\gamma_{ox,-}^{b,\pm})^3}{(\gamma_{ox,+}^{b,\pm})^3 (\gamma_{red,-}^{b,\pm})^2} \right). \quad (19)$$

In the current study, the formal potentials are assumed to be constant

and thus independent of the state of charge value as in the cell models studied in [16] and [25], a hypothesis discussed in Section 6.

5.2. Ohmic cell resistance

The overall Ohmic losses are given by

$$U_{\text{ohmic}} = I \cdot R_{\text{ohmic}} \quad (20)$$

where R_{ohmic} denotes the cell resistance, subsuming the electronic, ionic and membrane resistances and $I = i_{\text{mem}} A_{\text{mem}}$ is the total current at the electrode-membrane interface, where $A_{\text{mem}} = L_h L_w$ denotes the cross-sectional membrane area and i_{mem} is the corresponding current density.

5.3. Kinetic and concentration overpotentials

We model the electron transfer at the electrode with the semi-empirical Butler-Volmer expression [23,26]. The geometric current density in units of A cm⁻² is then given by

$$i_{\pm} = i_{0,\pm} \left(g_{\text{red},\pm}^c e^{(1-\beta_{\pm})/f \eta_{\text{tot},\pm}} - g_{\text{ox},\pm}^c e^{-\beta_{\pm}/f \eta_{\text{tot},\pm}} \right), \quad (21)$$

where $i_{0,\pm}$ is the exchange current density, β_{\pm} is the symmetry factor and $f^{-1} = RT/F \approx 25$ mV denotes the thermal voltage [27]. The exchange current density is given by

$$i_{0,\pm} = i_{0,\text{ref},\pm} \left(\frac{c_{\text{red},\pm}^b}{c_{\text{ref},\pm}^b} \right)^{\beta_{\pm}} \left(\frac{c_{\text{ox},\pm}^b}{c_{\text{ref},\pm}^b} \right)^{(1-\beta_{\pm})} \quad \text{with} \quad i_{0,\text{ref},\pm} = F k_{0,\pm} c_{\text{ref},\pm}^b, \quad (22)$$

where $k_{0,\pm}$ is a reaction constant in units of ms⁻¹ and $c_{\text{ref},\pm}^b$ denotes an arbitrary reference molar concentration in the electrolyte bulk. These reference values can be chosen conveniently as $c_{\text{ref},\pm}^b = 1$ mol L⁻¹. Furthermore,

$$g_{a,\pm}^c = \frac{c_{a,\pm}^s}{c_{a,\pm}^b} = 1 - \frac{\Delta c_{a,\pm}}{c_{a,\pm}^b} \quad \text{with} \quad c_{a,\pm}^b = c_{a,\pm}^s + \Delta c_{a,\pm} \quad (23)$$

describes the dependence of the forward and backward reaction rates on the concentration variation between the electrode surface and electrolyte bulk. The symmetry factor, β_{\pm} , satisfies $0 \leq \beta_{\pm} \leq 1$. Finally,

$$\eta_{\text{tot},\pm} = U_{\pm} - U_{\text{eq},\pm} \quad (24)$$

is the total overpotential in the half-cells.

The geometric electric current density, i_{\pm} , is assumed to be constant within each electrode, so that i_{\pm} related to the total cell current I by the simple relation

$$i_{\pm} = \pm \frac{I}{A_s} = \pm \frac{I}{a_s V_{\text{el}}}, \quad (25)$$

where $A_s = a_s V_{\text{el}}$ denotes the total electrode surface in each of the electrode compartments and $a_s = A_s / V_{\text{el}}$ is the specific electrode surface, defined as the ratio of the total electrode surface, A_s , and the electrode volume, V_{el} .

In the following we assume the symmetry factor in the Butler-Volmer Eq. (21) to be given by $\beta_{\pm} = 1/2$. In this case the exchange current density simplifies to

$$i_{0,\pm} = F k_{0,\pm} \sqrt{c_{\text{red},\pm}^b c_{\text{ox},\pm}^b} \quad (26)$$

and the total overpotential η_{tot} can be expressed explicitly in terms of the current density as

$$\eta_{\text{tot},\pm} = \frac{2}{f} \ln \left(\frac{i_{\pm} + \sqrt{i_{\pm}^2 + 4 g_{\text{ox},\pm}^c g_{\text{red},\pm}^c (i_{0,\pm})^2}}{2 g_{\text{red},\pm}^c i_{0,\pm}} \right). \quad (27)$$

5.4. Mass transport model

In the proximity of the electrode surface, a thin boundary layer is formed, in which steep concentration variations of the electroactive species can occur. By Faraday's law, the electric current density is balanced by a species mass flux density in the electrolyte, which is often assumed to be dominated by diffusion in the boundary layer [16]. As the current density is increased, the concentration of the reactant decreases at the electrode surface. In the limiting case of large electric current densities, the reactant concentration vanishes at the electrode surface and the electric current density reaches a limiting current density.

However, even well before reaching the limiting current, taking into consideration mass transport limitations of the species through the boundary layer is important as it directly affects the so-called concentration overpotential that occurs when the electrochemical reactions become limited by slow transport processes.

Assuming pure diffusive transport of the electrolyte within the vicinity of the electrode surface (a hypothesis discussed in Section 6) leads to the mass conservation equation

$$\nu_{a,\pm} \frac{i_{\pm}}{F} = -D_{a,\pm} (\mathbf{n} \cdot \nabla c_{a,\pm}), \quad (28)$$

where \mathbf{n} denotes a unit vector pointing from the electrolyte into the electrode domain.

The mass transfer coefficient, $k_{m,a,\pm}$, relates the difference in the bulk and surface electrolyte concentrations to the mass transfer at the surface by

$$k_{m,a,\pm} \Delta c_{a,\pm} = -D_{a,\pm} (\mathbf{n} \cdot \nabla c_{a,\pm}), \quad (29)$$

so that

$$\Delta c_{a,\pm} = \frac{\nu_{a,\pm} i_{\pm}}{F k_{m,a,\pm}} = \pm \frac{\nu_{a,\pm} I}{a_s V_{\text{el}} F k_{m,a,\pm}}. \quad (30)$$

In the extreme case of a complete depletion of reactants at the electrode surface we have $\Delta c_{a,\pm} = c_{a,\pm}^b$, so that the limiting current is given by

$$i_{a,\text{lim},\pm} = \nu_{a,\pm} F k_{m,\pm} c_{a,\pm}^b, \quad (31)$$

where we used $|\nu_{a,\pm}| = 1$.

The mass transfer coefficient k_m encodes the pore-scale transport of the electrode active species between the electrolyte bulk and the electrode surface. Typically, k_m is fitted to mass transport experiments. A simple model for the mass transfer coefficient is given by

$$k_m = a_m v^{b_m}, \quad (32)$$

where v is the superficial velocity and a_m, b_m denote experimentally determined fitting parameters [28–30].

5.5. Nondimensionalization

To nondimensionalize the above relations we introduce the dimensionless variables

$$\bar{c}_a = \frac{c_a}{c^0}, \quad \bar{\eta} = f \eta, \quad \bar{i} = \frac{i}{i^0}, \quad \bar{i}_0 = \frac{i_0}{i^0}, \quad (33)$$

where c^0 is a reference (bulk) molar concentration and i^0 denotes a characteristic current density given by

$$i^0 = \frac{F D^0 c^0}{l^0}, \quad (34)$$

where D^0 is a reference diffusivity and l^0 a characteristic pore length scale in the porous electrode.

The dynamics of the mass transfer and reaction kinetics are deter-

mined by the dimensionless scaling parameters

$$\text{Sh} = \frac{k_m l^0}{D^0}, \quad \text{Ki} = \frac{k_0 l^0}{D^0}, \quad (35)$$

where Sh denotes the Sherwood number and Ki is a kinetic number. The dimensionless limiting current and the exchange current density are then given by

$$\bar{i}_{a,\text{lim}} = \nu_a \bar{c}_a^b \text{Sh}, \quad \bar{i}_0 = \sqrt{\bar{c}_{\text{ox}}^b \bar{c}_{\text{red}}^b} \text{Ki} = \sqrt{|\bar{i}_{\text{ox},\text{lim}} \bar{i}_{\text{red},\text{lim}}|} \frac{\text{Ki}}{\text{Sh}}. \quad (36)$$

The total overpotential (27) is then given in nondimensional form by

$$\bar{\eta}_{\text{tot}} = 2 \ln \left(\frac{\bar{i} + \sqrt{\bar{i}^2 + 4 \bar{g}_{\text{ox}}^c \bar{g}_{\text{red}}^c (\bar{i}_0)^2}}{2 \bar{g}_{\text{red}}^c \bar{i}_0} \right) = 2 \text{arsinh} \left(\frac{\bar{i}}{2 \bar{i}_0 \sqrt{\bar{g}_{\text{ox}}^c \bar{g}_{\text{red}}^c}} \right) - \ln \left(\frac{\bar{g}_{\text{red}}^c}{\bar{g}_{\text{ox}}^c} \right) \quad (37)$$

$$= 2 \text{arsinh} \left(\frac{\bar{i} \cdot \text{Sh}}{2 \text{Ki} \sqrt{(\bar{i} + \bar{c}_{\text{ox}}^b \text{Sh})(\bar{c}_{\text{red}}^b \text{Sh} - \bar{i})}} \right) - \ln \left(\frac{\bar{c}_{\text{ox}}^b \bar{c}_{\text{red}}^b \text{Sh} - \bar{i}}{\bar{c}_{\text{red}}^b \bar{i} + \bar{c}_{\text{ox}}^b \text{Sh}} \right), \quad (38)$$

where we have used

$$\bar{g}_a^c = 1 - \frac{\nu_a \bar{i}}{\bar{c}_a^b \text{Sh}} = 1 - \frac{\bar{i}}{\bar{i}_{a,\text{lim}}}. \quad (39)$$

In the limiting case of small electric current densities Eq. (38) reduces to

$$\begin{aligned} \bar{\eta}_{\text{tot}} &= \left(\frac{1}{\bar{c}_{\text{red}}^b \text{Sh}} + \frac{1}{\bar{c}_{\text{ox}}^b \text{Sh}} + \frac{1}{\sqrt{\bar{c}_{\text{ox}}^b \bar{c}_{\text{red}}^b} \text{Ki}} \right) \bar{i} + O(\bar{i}^2) \\ &= \left(\frac{1}{\bar{i}_{\text{red},\text{lim}}} - \frac{1}{\bar{i}_{\text{ox},\text{lim}}} + \frac{1}{\bar{i}_0} \right) \bar{i} + O(\bar{i}^2), \end{aligned} \quad (40)$$

see e.g. Bard and Faulkner [23] on p. 106.

5.6. Activation and concentration overpotentials

Let us consider the case of fast mass transport, i.e. $\text{Sh} \rightarrow \infty$. Then Eq. (39) reduces to $\bar{g}_a^c = 1$ so that concentration variations between bulk and surface vanish and the total overpotential (38) simplifies to the activation overpotential

$$\bar{\eta}_{\text{act}} = 2 \ln \left(\frac{\bar{i} + \sqrt{\bar{i}^2 + 4 \bar{i}_0^2}}{2 \bar{i}_0} \right) = 2 \text{arsinh} \left(\frac{\bar{i}}{2 \bar{i}_0} \right), \quad (41)$$

see e.g. [16,31]. The concentration overpotential is then determined by

$$\bar{\eta}_{\text{conc}} = \bar{\eta} - \bar{\eta}_{\text{act}}. \quad (42)$$

In the limit of large exchange current densities, i.e. $\text{Ki} \rightarrow \infty$, we find that the total overpotential converges to the concentration overpotential as expected, as

$$\bar{\eta} = \bar{\eta}_{\text{conc}} + O(\text{Ki}^{-1}) = \ln \left(\frac{\bar{g}_{\text{ox}}^c}{\bar{g}_{\text{red}}^c} \right) + O(\text{Ki}^{-1}), \quad (43)$$

whereas in the limit of small exchange current densities, i.e. $\text{Ki} \rightarrow 0$, the concentration overpotential simplifies to

$$\bar{\eta}_{\text{conc}} = \begin{cases} -2 \ln(\bar{g}_{\text{red}}^c) + O(\text{Ki}^2), & \bar{i} > 0, \\ 2 \ln(\bar{g}_{\text{ox}}^c) + O(\text{Ki}^2), & \bar{i} < 0. \end{cases} \quad (44)$$

The expression in Eq. (44) was used in [16] to define the concentration overpotential.

5.7. Discussion

The assumption of the symmetry factor to be given by $\beta = 0.5$ allows for an explicit formulation of the total overpotential and thus the cell voltage in terms of SoC and current density. To gain insight into the general form of the total overpotential we have performed a dimensional analysis, which reveals the dependency of the overpotential on the mass transfer and kinetic reaction rates and allows recovering activation and concentration overpotentials as limiting cases.

The analysis presented in the previous section is based on the Butler-Volmer equation formulated in terms of bulk concentrations. An alternative representation of the Butler-Volmer equation expressed in terms of surface quantities given by

$$i_{\pm} = i_{0,\pm}^s (e^{(1-\beta_{\pm})f\eta_{\text{tot},\pm}} - e^{-\beta_{\pm}f\eta_{\text{tot},\pm}}) \quad \text{with} \quad i_{0,\pm}^s = k_{0,\pm} \left(\bar{c}_{\text{red},\pm}^s \right)^{\beta_{\pm}} \left(\bar{c}_{\text{ox},\pm}^s \right)^{(1-\beta_{\pm})} \quad (45)$$

yields instead a surface overpotential η_{\pm}^s . The total overpotential $\eta_{\text{tot},\pm}$ with respect to bulk quantities is then related to the surface overpotential η_{\pm}^s by

$$\eta_{\text{tot},\pm} = \eta_{\pm}^s + \eta_{\text{ref},\pm}, \quad (46)$$

where $\eta_{\text{ref},\pm}$ denotes the polarization with respect to bulk quantities, as shown in Appendix D.

6. Model validity range

The range of validity of the 0D-U-I-SoC model is impacted by the modelling assumptions, such as the assumption of negligible spatial concentration variations of electroactive species along the forced convection direction through the porous electrodes. In this section we discuss the implications of the most crucial assumptions on the range of model validity.

6.1. Spatial concentration variations

Let c_a^{in} and c_a^{out} denote the bulk molar concentrations of species a at the electrode inflow and outflow boundaries within a half-cell. For the macroscopic spatial concentration variations of species a through the porous electrode to be negligible we require

$$|c_a^{\text{in}} - c_a^{\text{out}}| \ll c_a^{\text{avg}}, \quad (47)$$

where c_a^{avg} is the arithmetic average concentration defined in Eq. (8). As shown in [15], the relative spatial concentration variation between inflow and outflow boundaries is given by the dimensionless parameter

$$\Lambda_{c_a} = \frac{|c_a^{\text{in}} - c_a^{\text{out}}|}{c_a^{\text{avg}}} = \frac{|i_{\text{mem}}| A_{\text{mem}}}{F \dot{V} c_a^{\text{avg}}}, \quad (48)$$

where i_{mem} denotes the electric current density with respect to the membrane cross-sectional area and \dot{V} is the volumetric flow rate. The requirement (47) is thus equivalent to $\Lambda_{c_a} \ll 1$.

At large absolute current densities, the supply of reactants to the electrode surface becomes the limiting factor. The active validity constraint is then given by the reactant species with the smallest average molar concentration in the two electrode compartments. Thus, the overall constraint is $\Lambda_c \ll 1$ with

$$\Lambda_c = \begin{cases} \max\{\Lambda_{c_{\text{ox},-}}, \Lambda_{c_{\text{red},+}}\} & \text{for } i_{\text{mem}} \geq 0, \\ \max\{\Lambda_{c_{\text{ox},+}}, \Lambda_{c_{\text{red},-}}\} & \text{else.} \end{cases} \quad (49)$$

Clearly, the requirement $\Lambda_c \ll 1$ can be formulated in terms of the electric current density as

$$|i_{\text{mem}}| = \Lambda_c \frac{F \dot{V} c^{\text{avg}}}{A_{\text{mem}}} \ll \frac{F \dot{V} c^{\text{avg}}}{A_{\text{mem}}}, \quad (50)$$

where c^{avg} is average concentration of the species that maximizes Λ_c in Eq. (49). Therefore, the model validity requires the electric current density, $|i_{\text{mem}}|$, to be small enough, depending on the volumetric flow rate, \dot{V} , the average species concentration, c^{avg} , and the membrane area, A_{mem} .

6.2. Formal potential

As discussed in Section 5, the formal potentials are defined as

$$U'_{\text{eq},\pm} = U^*_{\text{eq},\pm} - \frac{RT}{F} \ln \left(\frac{\gamma_{\text{red},\pm}^b}{\gamma_{\text{ox},\pm}^b} \right). \quad (51)$$

In most of the literature and textbooks, see e.g. [23], the experimental conditions are often assumed to be comparable to classical Cyclic Voltammetry (CV) or Rotating Disk Electrodes (RDE) experiments, where dilute solutions of active materials ($[10^{-4}, 10^{-3}]$ mol/L) are present in a large excess of supporting electrolyte.

In this concentration range, it is reasonable to make the dilute solution hypothesis, such that the relationship between activity and concentration follows the Debye-Hückel limiting law [32] and the ratio $\gamma_{\text{red},\pm}^b / \gamma_{\text{ox},\pm}^b$ remains close to 1. However, in flow batteries, the active material concentrations vary greatly during battery cycling (up to several moles per liter), rendering the dilute solution hypothesis and the Debye-Hückel limiting law invalid.

While it is common practice to consider a constant value for the formal potential [16], the activity coefficients of the oxidised and reduced species are in general different and their values will depend on the concentration of each specie, such that the formal potential should formally be given as a function of the SoC. As demonstrated in Section 8, the formal potential is one of the most important parameters in cell voltage predictions, and more rigorous modelling of concentrated solution behaviour may be required in future flow battery models.

6.3. Temperature variations

All experiments were conducted in a small thermostated room, however temperature increases are possible in the reservoirs due to Joule heating of the membrane, particularly at high current densities during the polarisation experiment. For this reason, we report in Fig. 9b the results of the same polarisation experiment (at 20% SoC) as in Fig. 9a with larger reservoirs (100 mL instead of 10 mL) placed in 1 L supporting water baths, in order to increase the total heat capacity of the system and reduce potential temperature variations. As expected, the discrepancy between model and experiment was lower at higher current in the case of Fig. 9b, indicating that a small increase in temperature affects the cell voltage.

The sensitivity analysis conducted in Section 8 confirmed that the model is indeed sensitive to temperature variations, and the experimental setup should be chosen carefully when greater accuracy is required, especially at higher currents.

6.4. Cell resistance

In the present model, the ohmic cell resistance was assumed constant within a range of uncertainty determined by EIS measurements conducted before and after the experiments.

The main ohmic contribution coming from the ion-exchange membrane, which conductivity is a function of the temperature and the external electrolyte, the cell resistance should formally be measured as a function of the temperature and the SoC for greater accuracy.

6.5. Membrane permselectivity

To allow for a simpler coupling between state of charge and concentration, the membrane permselectivity was assumed equal to one, i.e. only chloride ions were considered to cross the membrane. This hypothesis was justified by the absence of supporting electrolyte (implying the absence of small co-ions travelling through the membrane due to migration) and the typically higher permselectivity of anion-exchange membranes compared to cation-exchange membranes. Membrane permselectivity has, however, an impact on Faradaic efficiency, since active cations crossing the membrane may lead to a discrepancy between the measured electronic current density and the effective ionic current density, defined as the flux of chloride ions through the membrane times the Faraday constant.

An imperfectly permselective membrane could partly explain the asymmetry observed on the charge/discharge plots of Fig. 7, which seem to suggest that the cell resistance is higher during discharge (or, equivalently, that the effective current is lower during discharge). It could also explain the discrepancies observed on the polarisation plots of Fig. 9 at high current densities or on the voltage efficiency plots of Fig. 8, which seem to indicate that the model under-estimates the cell resistance in this region (or, equivalently, that it over-estimates the effective current density).

The transfer of hydrated cations through the membrane could also have an impact on the experimentally measured electro-osmotic coefficient, although (as justified in Section 8) this parameter has a relatively small impact on the time scales considered in the present work.

6.6. Mass transfer

In classical electrochemistry textbooks, such as [23], the transport in the Nernst layer is frequently assumed to be diffusion-dominated. While this is likely to be the case in experiments where the supporting electrolyte is greatly in excess with respect to the active materials, in flow batteries the ratio between supporting electrolyte and active material concentrations rarely exceeds 3 (in the system considered in this work, there is no supporting electrolyte).

This leads to transport equations in the Nernst layer that are likely to be more complex in practice than a simple Fick's law, as migration and other driving forces may not be negligible. As shown in Section 8, two parameters correlated to transport in the diffusion layer (namely mass transport coefficient a_m and flow rate \dot{V}) contribute significantly to the model predictions, implying that greater accuracy could be achieved by revisiting equations of transport in the Nernst diffusion layer.

7. Experimental model validation

Cell voltage and power density predictions are presented for the TEMPTMA/MV system over a range of electric current density and state of charge values, as well as model validation results of charge-discharge and polarization experiments.

Table 3 shows the chemical and material properties that we used in the model evaluations.

Literature values were taken for the specific electrode surface area and the reaction constants for the TEMPTMA/MV system reported by Janoschka et al. [1]. The electro-osmotic drag coefficient was taken as the size of the solvation shell of Chloride ions [20], as justified in Section 4.

Due to large experimental uncertainties in the estimation of the formal half-cell potential of Methyl Viologen, we have fitted E'_{MV} to OCV measurements.

Mass transfer coefficients reported in literature show great variability [28,29,33], which can be attributed to the experimental design, as well as the variability of the electrolyte transport properties and the pore-scale structures of the examined porous electrodes. For this reason

Table 3
Chemical and material properties.

Parameter Description	Symbol	Value	Source
Specific electrode surface area	a_s	$2 \times 10^5 \text{ m}^{-1}$	Murthy et al. [16]
Formal half-cell potential of MV	$\Delta\phi'_{\text{eq},-}$	-0.66 V	Fitted
Formal half-cell potential of TEMPTMA	$\Delta\phi'_{\text{eq},+}$	0.62 V	Measured
Reaction constant in neg. electrode	$k_{0,-}$	$3.3 \times 10^{-5} \text{ m/s}$	Janoschka et al. [1]
Reaction constant in pos. electrode	$k_{0,+}$	$4.2 \times 10^{-5} \text{ m/s}$	Janoschka et al. [1]
Mass transport coefficient 1	a_m	$3.5 \times 10^{-5} (\text{m/s})^{0.1}$	Fitted
Mass transport coefficient 2	b_m	0.9	Murthy et al. [16]
Electro-osmotic drag	κ_s	6	Ge et al. [20]

we have fitted the mass transfer coefficient a_m used in the empirical mass-transfer coefficient model Eq. (32) to polarization experiments of the TEMPTMA/MV system.

7.1. Model evaluation

Figure 6 shows model predictions of the cell voltage and power density

$$p_{\text{mem}} = i_{\text{mem}} \cdot U_{\text{cell}}, \quad (52)$$

where $i_{\text{mem}} = I/A_{\text{mem}}$ denotes the current density, over a wide range of current density and state of charge values using the test cell parameters given in Table 3. Thanks to the fast evaluation of the model, these plots can be generated quickly and provide insight in the cell performance in terms of operating conditions.

In the plot of Fig. 6, we have indicated the isocurves of the dimensionless numbers $\Lambda_c = 10^{-2}$ and $\Lambda_c = 10^{-1}$ by a dotted and dashed curve, respectively. Generally, we expect the model validity to break down for $\Lambda_c \sim 1$ due to non-negligible spatial concentration variations as discussed in Section 6.1.

7.2. Charge-discharge experiments

Figure 7 shows the experimentally measured voltage for charge-discharge cycling experiments at constant charging and discharging

currents of 80 mA cm^{-2} and 120 mA cm^{-2} , together with the model predictions.

EIS measurements were performed before and after cycling, yielding an initial cell resistance of $348 \text{ m}\Omega$, and $360 \text{ m}\Omega$ after cycling. The model was evaluated at both resistance values to estimate the resulting uncertainty in the model predictions as shown in Fig. 7.

A comparison of the model predictions with the experimental values shows that the model slightly underestimates the voltage for a charging current and overestimates the voltage for a discharging current, but allows for a good approximation of the voltage for both considered electric current densities.

The model allows predicting the voltage efficiency

$$\text{VE} = \frac{\oint U_{\text{cell}}^{\text{discharge}} dt}{\oint U_{\text{cell}}^{\text{charge}} dt}, \quad (53)$$

where the integration is performed over a whole charge-discharge cycle and

$$U_{\text{cell}}^{\text{discharge}} = \begin{cases} U_{\text{cell}}, & I < 0 \\ 0, & I \geq 0 \end{cases}, \quad U_{\text{cell}}^{\text{charge}} = \begin{cases} 0, & I < 0 \\ U_{\text{cell}}, & I \geq 0 \end{cases} \quad (54)$$

denote the discharging and charging voltages, respectively. Figure 8 shows the predicted voltage efficiencies as a function of the electric current density, where the cutoff voltages have been set to 0.9 V and 1.5 V , respectively. The predicted voltage efficiencies are plotted for both values of the measured cell resistance values to indicate the implied uncertainty. A comparison with the voltage efficiencies obtained from the charge-discharge cycling curves included in Fig. 7 reveals that the model slightly overestimates the voltage efficiency.

7.3. Polarization experiments

Several polarization experiments were performed at different values of the SoC for model validation. Figure 9 shows both the measured cell voltage and power density as a function of the current density for several polarization experiments performed at SoC 20%, 50% and 100%, respectively.

Cell resistance values were measured by EIS experiments before and after cycling, see Table 4. To account for the uncertainty in the cell resistance the model was evaluated both at the minimum and maximum value of the cell resistance to give uncertainty intervals on both the cell voltage and the power density.

The usage of a finite electrolyte volume results in non-negligible

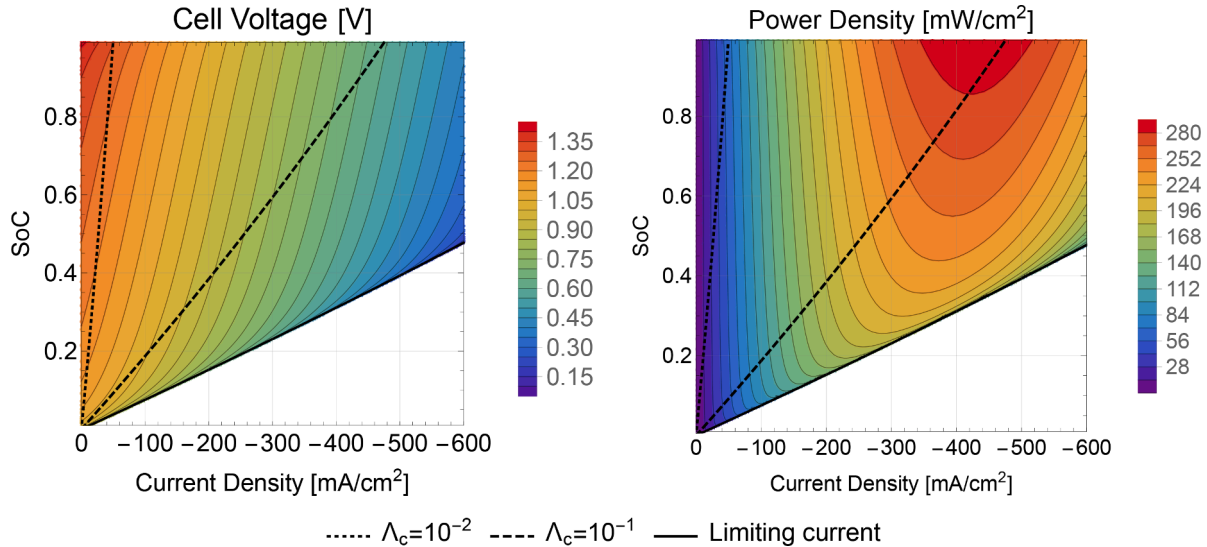


Fig. 6. Model predictions of the cell voltage (left) and power density (right) as a function of the SoC and current density.

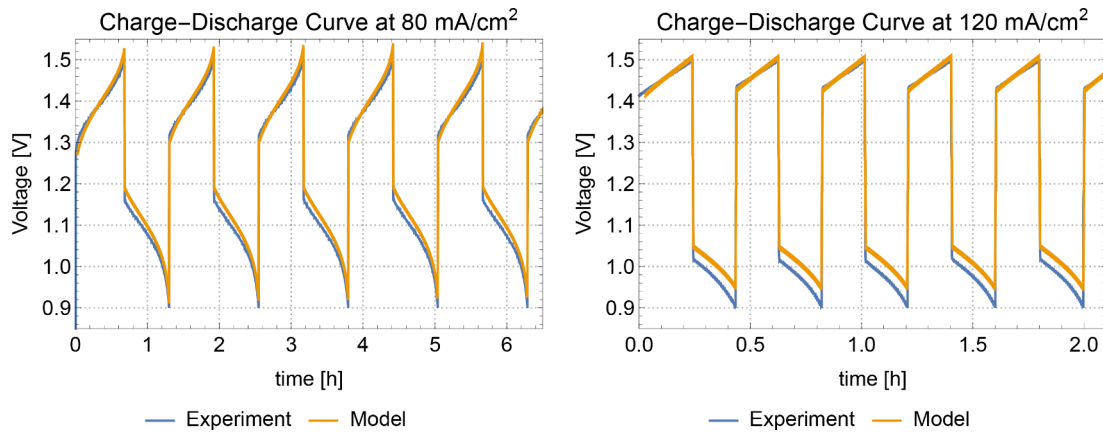


Fig. 7. Charge-discharge experiments at 80 mA cm⁻² and 120 mA cm⁻².

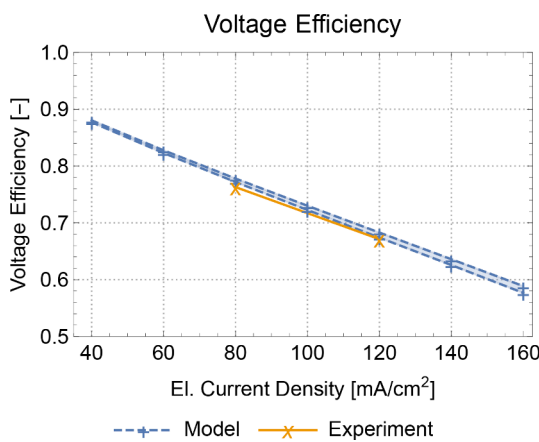


Fig. 8. Voltage efficiencies over a range of current densities predicted by the model, together with experimental measurements.

changes of the SoC during the discharging periods over which the voltage is sampled. To account for the change in the SoC, the model is evaluated both at the initial target SoC and the lowest expected SoC resulting from the discharging of the electrolyte. The lowest and highest predicted cell voltage and power density values for a given current density found over the range of possible cell resistance and SoC values yield uncertainty ranges that are shown by the orange shaded regions in Fig. 9.

Similarly, we account for the uncertainty in the voltage measurements by assuming normally distributed voltage sample values, from which we evaluate 95% confidence intervals, which are indicated by the blue shaded regions in Fig. 9.

A comparison with the experimental values shows promising agreement of the model predictions up to the model validity threshold value of $\Lambda_c = 10^{-1}$ beyond which the predicted voltage and power density start to deviate more strongly and the assumption of negligible concentration variations breaks down. For higher values of the SoC the model validity extends to larger (negative) current densities due to higher molar concentrations of the reactants. This allows the model to accurately predict the voltage and power density at SoC = 100% up to $|i_{\text{mem}}| = 500 \text{ mA cm}^{-2}$, whereas the model prediction at SoC = 20% starts to deviate significantly from the experimental measurements beyond $|i_{\text{mem}}| = 115 \text{ mA cm}^{-2}$.

8. Sensitivity analysis

A sensitivity analysis was carried out to assess the impact of different

input parameters on the model, which is useful not only to detect possible limitations of the model hypothesis, but also to quantify which material parameters or design choices have the greatest influence on battery performance.

A local sensitivity analysis was carried out on the model using the Morris method [34], chosen for its efficiency and simplicity regarding input distributions. The elementary effects $d_i^{(j)}$ of each input parameter on the cell voltage U_{cell} are approximated as a finite difference

$$d_i^{(j)} \approx \frac{U_{\text{cell}}(x_1^{(j)}, \dots, x_i^{(j)}(1 + \delta/2), \dots, x_n^{(j)}) - U_{\text{cell}}(x_1^{(j)}, \dots, x_i^{(j)}(1 - \delta/2), \dots, x_n^{(j)})}{\delta \cdot x_i^{(j)}} \quad (55)$$

where δ is a perturbation parameter and the $x_i^{(j)}$ are samples of input parameters, obtained from Monte-Carlo sampling in a 7-dimensional space of uniformly distributed variables. Reasonable ranges for the sampling of the different parameters were gathered in Table 5 and determined as follows: the resistance values were the extreme values reported in the previous tables of the manuscript (rounded). The formal potentials were measured experimentally (see acknowledgements) and observed to vary drastically for the MV electrolyte. Values reported on Table 5 were the extreme measured values (rounded). The flow rate was measured in dedicated tests with our peristaltic pumps. The reaction rate k_0 variation range was taken as two orders of magnitude such that uncertainties arising from experimental measurement, as well as possible electrode pre-treatments were accounted for. The electro-osmotic coefficient was taken between 0 (no transfer) and 6 (size of the hydration shell of chloride ions [20]).

As the different input parameters vary greatly in terms of units and values, non-dimensional elasticities were defined from elementary effects as

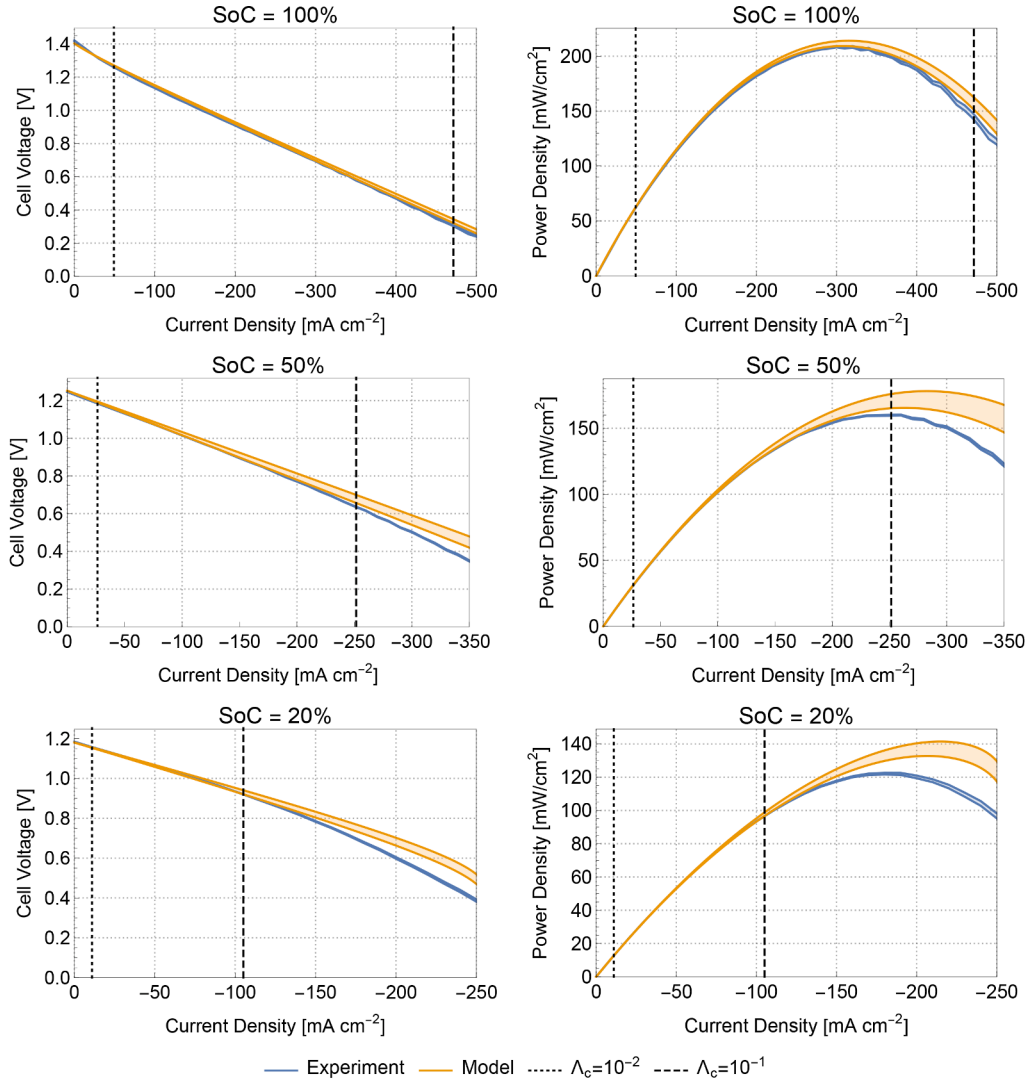
$$s_i^{(j)} = \left| \frac{d_i^{(j)} x_i^{\text{ref}}}{U_{\text{cell}}^{\text{ref}}} \right|, \quad (56)$$

from which the Morris parameters

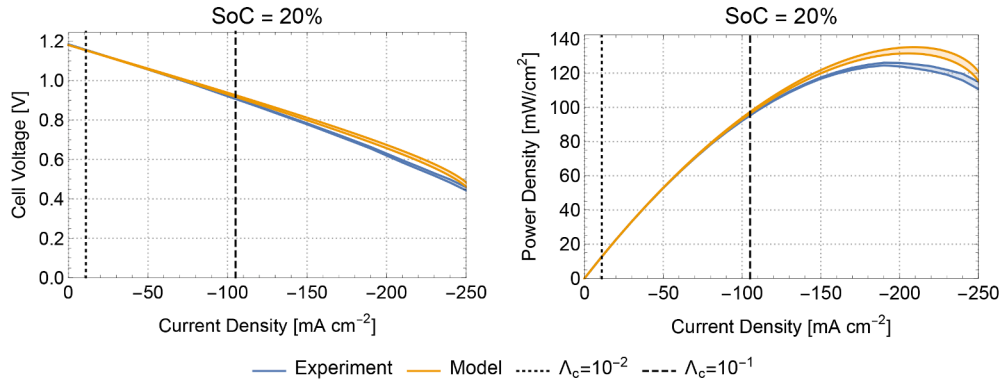
$$\mu_i = \frac{1}{n} \sum_{j=1}^n s_i^{(j)}, \quad \sigma_i^2 = \frac{1}{n-1} \sum_{j=1}^n (s_i^{(j)} - \mu_i)^2 \quad (57)$$

were calculated as the mean and variance of the elasticity distribution using $n = 10^3$ samples.

All calculations were carried out at a state of charge of 50% for different current densities. Results of the Morris parameters plotted in the (μ_i, σ_i) plane are presented in Fig. 10 and yield the following result in terms of parameter influence on the cell voltage, at a current density of 80 mA cm⁻²:



(a) Polarization experiments performed with 10 mL electrolyte solution.



(b) Temperature, SoC and flow rate-controlled polarization experiments performed with 100 mL electrolyte solution.

Fig. 9. Measured voltage and power densities of polarization experiments, together with the model predictions.

$$k_0 < \kappa_s < \dot{V} \approx T < R_{\text{ohmic}} < U'_{\text{eq},+}. \quad (58)$$

The dominant term appears to be the formal potential $U'_{\text{eq},+}$, which was expected due to its direct influence on the cell voltage. This further illustrates how activity coefficients and concentrated solution behavior

may have an impact on cell parameters, and should rigorously be modeled as a function of the SoC. The cell resistance R_{ohmic} also has a high influence on the model, and becomes more important as the current density becomes higher, which is expected due to its direct influence on the ohmic term. The cell resistance being dominated by the membrane contribution, it illustrates the importance of the ion-exchange

Table 4

Measured cell resistance values before and after the polarization experiments.

State of Charge	Cell Resistance Before	Cell Resistance After
20%	398 mΩ	437 mΩ
50%	443 mΩ	409 mΩ
100%	409 mΩ	399 mΩ

Table 5

Input parameters and reasonable ranges of variation for the sensitivity analysis.

Input parameter	Symbol	Unit	Reference	Range
Formal potential	$U_{eq,+}^{\circ}$	V	0.62	[0.6, 0.7]
Cell resistance	R_{ohmic}	mΩ	286	[250, 450]
Reaction constant	k_0	m/s	$3.3 \cdot 10^{-5}$	$[3.3 \cdot 10^{-6}, 3.3 \cdot 10^{-4}]$
Electro-osmotic coefficient	κ	-	6	[0, 6]
Flow rate	\dot{V}	mL/min	16	[15, 17]
Temperature	T	K	298.15	[298, 302]

membrane conductivity in flow battery performance.

The flow rate \dot{V} and the mass transfer coefficient a_m seem to have a significant influence on the model and a rather high variance, indicating higher interactions or nonlinearities, which increase as the current density is increased. As mentioned in Section 6, Fickian diffusion may be insufficient to correctly characterise transport phenomena in the Nernst layer, and future extensions of the model will put the emphasis on improving transport equations in this region.

The temperature T also has a significant impact on the model, as mentioned in Section 6 and experimentally observed in Fig. 9b and a. This further illustrates that rigorous non-isothermal models are required to correctly predict battery behavior in real-life applications.

The electro-osmotic drag coefficient κ_s has a relatively minor impact on the model, which makes sense since it only weakly affects the concentrations of active materials on each side. The reaction constant k_0 has the smallest impact on the model, despite a range of variation spanning two orders of magnitude.

9. Code availability

The 0D-U-I-SoC model has been implemented in Mathematica 12 and published as open-source software under the 3-clause BSD license, allowing for a full inspection of the model. The software is maintained on the GitHub account *ISOMORPH-Electrochemical Cells*, from where it can be obtained. The open-source model implementation can serve as a point of departure for further specific model adaptations and extensions. Furthermore, being published under the 3-clause BSD license also allows the model to be used commercially.

10. Conclusions

The physics-based 0D-U-I-SoC model presented in this paper allows for efficient single-cell performance predictions of aqueous organic flow batteries. Thanks to the low computational cost of the model, parameter studies and optimizations can be readily performed, even with limited computational resources.

The fundamental assumption of negligible spatial variations of the electrolyte bulk composition within each electrode compartment allows for a dimensionality reduction to 0D. As shown by Sharma et al. [15], this assumption is valid for typical cell geometries and operating conditions reported in the literature. However, it requires the electric current to be small, depending on the cell geometry, electrolyte concentration, and flow rate as discussed in Section 6.

Similar to Murthy et al. [16] we assume the symmetry factor in the Butler-Volmer equation for single-step reactions to be given by $\beta = 0.5$. This simplifying assumption allows for an explicit expression of the overpotential in terms of the applied current density. An extension to general symmetry coefficients is possible, but would result in an implicit formulation of the overpotential.

The performed experimental model validations on the TEMPTMA/MV system show that the model allows for quantitatively accurate performance predictions within its range of validity. Based on a sensitivity study with 2000 evaluations, the estimated run time of a single voltage evaluation is 1.3×10^{-3} ms on a 2019 MacBook Pro laptop with a 2.4 GHz 8-Core Intel Core i9 processor. The model accuracy, together with its low computational cost are, to the best of our knowledge, reported for the first time in the aqueous organic flow battery literature.

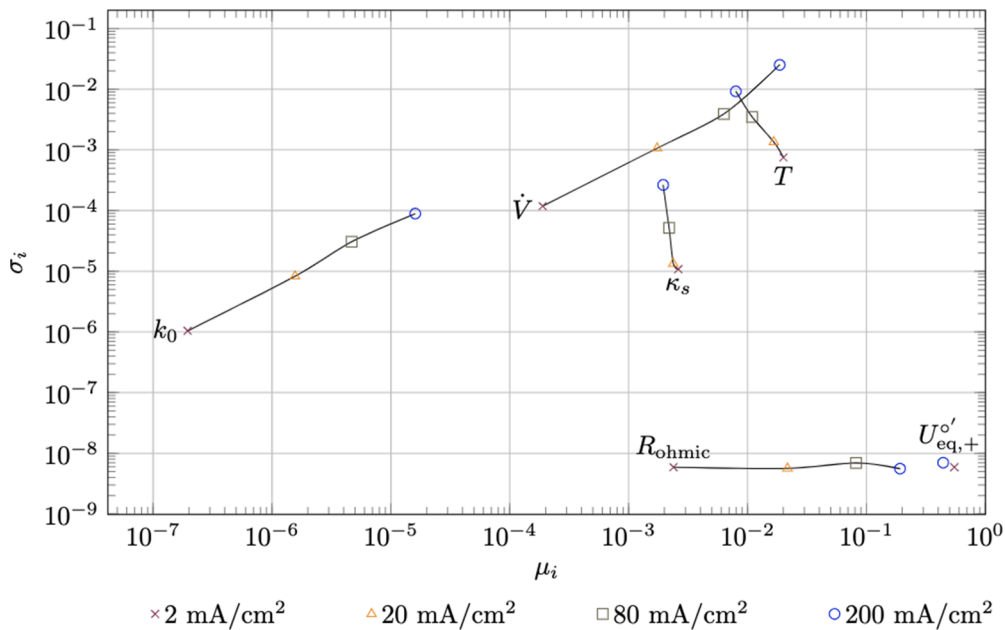


Fig. 10. Representation of the sensitivity analysis in the Morris plane. High values on the x-axis indicate parameters with high influence, high values on the y-axis indicate parameters with high interaction and/or nonlinearities.

As expected, the model predictions deviate from the experimental values for large absolute current densities, since several assumptions of the model discussed in Section 6 may break down in these conditions. Other disregarded processes, such as possible temporal temperature variations, diffusion of electroactive species through the membrane, or non-negligible side reactions could further contribute to the observed discrepancy between the model predictions and the experimentally determined voltage and power densities.

We intend to extend the range of validity of the presented model in

future works by including concentration-dependent formal potentials based on experimental measurements of activity coefficients, improved modelling of the coupled process of flow and mass transport in the porous electrodes and consideration of additional transport phenomena through ion-exchange membranes.

Table of Symbols

Table 6

List of symbols used in the publication.

Symbol	Description	Unit
a_α	Activity of species α	—
a_s	Specific electrode surface area	m^{-1}
A_{mem}	Cross-sectional membrane area ($A_{\text{mem}} = L_w L_h$)	m^2
A_s	Total electrode surface area ($A_s = V_{\text{el}} a_s$)	m^2
c_α	Molar concentration of species α	mol L^{-1}
D_α	Diffusion coefficient of species α	$\text{m}^2 \text{s}^{-1}$
D^0	Characteristic (or reference) diffusion coefficient	$\text{m}^2 \text{s}^{-1}$
i	Geometric electric current density (I/A_s)	A m^{-1}
\bar{i}	Dimensionless geometric electric current density ($\bar{i} = i/i^0$)	—
i^0	Characteristic geometric electric current density	A m^{-2}
i_0	Exchange current density	A m^{-2}
\bar{i}_0	Dimensionless exchange current density ($\bar{i}_0 = i_0/i^0$)	—
i_{mem}	Electric current density with respect to the membrane cross-sectional area (I/A_{mem})	A m^{-2}
I	Total electric current	A
n_α	Number of moles of species α	mol
f	Inverse thermal voltage ($f = F/(RT)$)	V^{-1}
F	Faraday constant	C mol^{-1}
K_i	Kinetic number ($K_i = k_0 l^0 / D^0$)	—
l^0	Characteristic length scale at the pore-scale	m
L_{el}	Thickness of electrode compartment (in through-plane direction)	m
L_m	Thickness of the membrane (in through-plane direction)	m
L_h	Height of the electrochemical cell	m
L_w	Width of the electrochemical cell	m
\mathbf{n}	Normal vector	—
Q	Total available charge	A h
Q_R	Reaction quotient of the overall cell reaction	—
R	Universal gas constant	$\text{JK}^{-1} \text{mol}^{-1}$
R_{ohmic}	Overall cell resistance	Ω
SoC	State of charge of the battery	—
Sh	Sherwood number ($\text{Sh} = k_m l^0 / D^0$)	—
T	Temperature	K
U^*	Formal potential	V
U_{OCV}	Open circuit voltage	V
U_{ohmic}	Total cell voltage	V
\dot{V}	Volumetric flow rate	$\text{m}^3 \text{s}^{-1}$
VE	Voltage efficiency	—
V_{el}	Total electrode compartment volume ($V_{\text{el}} = L_{\text{el}} L_w L_h$)	m^3
$\tilde{V}_{m,\alpha}$	Apparent molar volume of species α	L mol^{-1}
\mathbf{v}	Superficial velocity	m s^{-1}
Greek symbols	Description	Unit
β	Butler-Volmer symmetry coefficient	—
γ_α	Activity coefficient of species α	—
ϵ_p	Porosity of the electrode	—
η_{tot}	Total overpotential	V
$\bar{\eta}$	Dimensionless overpotential ($\bar{\eta} = \eta f$)	—
η_{act}	Activation overpotential	V
η_{conc}	Concentration overpotential	V
κ_s	Electro-osmotic drag coefficient	—
Λ_c	Model validity parameter indicating relative concentration variations	—
μ_α	Chemical potential of species α	J mol^{-1}
Subscripts	Description	Unit
α	Refers to specific species, where $\alpha = 0$ denotes the solvent	—
\pm	Refers to positive (+) and negative (−) half-cell, respectively	—
Superscripts	Description	Unit
b	Refers to bulk quantity	—
s	Refers to surface quantity	—

Acknowledgements

This project has received funding from the European Union's Horizon 2020 research and innovation programme under Grant Agreement no. 875489 (SONAR) and 765289 (FlowCamp).

We would like to thank our many colleagues from JenaBatteries GmbH: Fritz Wernicke for the interesting discussions on the TEMPTMA/MV system and providing inputs such as Fig. 2, Raphael Hornung and Korcan Percin for the discussions on modelling aspects and membrane

transport, which will be featured in future works.

We would also like to thank Mathieu Beaucamp from the University of Lille, who performed experiments on the formal potentials of Methyl viologen electrolyte, which may deserve a separate paper.

Declaration of Competing Interest

The authors declare no conflict of interest.

Appendix A. Determination of molar volumes

Let us first consider a binary mixture of one dissolved salt in water. The molar volume of the pure solvent is given by

$$V_{m,0}^* = \frac{M_0}{\rho_0^*}, \quad (\text{A.1})$$

where ρ_0^* is the mass density of the solvent. The volume of the binary mixture can be stated as

$$V_{\text{mix}} = n_0 V_{m,0}^* + n_\alpha \tilde{V}_{m,\alpha}, \quad (\text{A.2})$$

where $\tilde{V}_{m,\alpha}$ denotes the apparent molar volume of species α . Dividing this relation by the volume yields the constraint

$$1 = c_0 V_{m,0}^* + c_\alpha \tilde{V}_{m,\alpha}. \quad (\text{A.3})$$

Analogously, the mixture density satisfies

$$\rho_{\text{mix}} = M_0 c_0 + M_\alpha c_\alpha. \quad (\text{A.4})$$

Solving the above relation for c_0 and plugging the result into the constraint (A.3) allows evaluating $\tilde{V}_{m,\alpha}$ in terms of the measured mixture density shown in Fig. 3. Here we model the binary mixture mass density as a linear function in terms of the molar species concentration, which implies that the resulting apparent molar volumes are constant with respect to the salt concentration.

For simplicity, we assume that the apparent molar volumes determined for binary mixtures well approximate the molar volumes in the battery, where we have in each half-cell a ternary mixture of solvent and two dissolved salts. The total electrolyte volume in the half-cells is then modelled as

$$V_{\text{mix},\pm} = n_{0,\pm} V_{m,0}^* + n_{\text{red},\pm} \tilde{V}_{\text{red},\pm} + n_{\text{ox},\pm} \tilde{V}_{\text{ox},\pm}. \quad (\text{A.5})$$

Appendix B. Initial molar concentrations

The initial state of the electrolyte is given by the total electrolyte volume V_\pm and the molar concentrations $c_{\text{ox},-}$ and $c_{\text{red},+}$ of the dissolved electroactive species in the negolyte and posolyte, respectively. The initial molar concentrations of the solvent in the two half-cells are determined by the given molar concentrations of the electroactive species and estimations of the molar and apparent molar volumes as

$$c_{0,-} = \frac{1 - c_{\text{ox},-} \tilde{V}_{m,\text{ox},-}}{V_{m,0}^*}, \quad c_{0,+} = \frac{1 - c_{\text{red},+} \tilde{V}_{m,\text{red},+}}{V_{m,0}^*}. \quad (\text{B.1})$$

Appendix C. Derivation of open-circuit membrane potential

The electrochemical potential of a species α in the electrolyte is given by

$$\tilde{\mu}_{\alpha,\pm} = \mu_{\alpha,\pm} + z_{\alpha,\pm} F \phi_\pm, \quad (\text{C.1})$$

where $\mu_{\alpha,\pm}$ denotes the chemical potential and ϕ_\pm is the electrostatic potential. Similarly, the electrochemical potential of electrons in the solid electrodes can be defined by del Olmo et al. [22]

$$\tilde{\mu}_{e,\pm} = -F \Phi_\pm, \quad (\text{C.2})$$

where Φ_\pm denotes the electric potential in the solid phase. In thermodynamic equilibrium, the electrochemical potential gradients vanish, so that we have

$$\tilde{\mu}_{\text{red},\pm} = \tilde{\mu}_{\text{ox},\pm} - F \Phi_\pm \quad (\text{C.3})$$

at the electrode surfaces. Additionally, for an anion-exchange membrane considered here, the negatively charged Chloride ions equilibrate across the membrane, so that

$$\tilde{\mu}_{\text{Cl}^-, -} = \tilde{\mu}_{\text{Cl}^-, +}. \quad (\text{C.4})$$

The open circuit potential is then given by

$$U_{\text{OCV}} = \Phi_+ - \Phi_- = \frac{1}{F} ((\tilde{\mu}_{\text{ox},+} - \tilde{\mu}_{\text{red},+}) - (\tilde{\mu}_{\text{ox},-} - \tilde{\mu}_{\text{red},-})), \quad (\text{C.5})$$

$$= U_{\text{eq},+} - U_{\text{eq},-} + U_{\text{eq},m}, \quad (\text{C.6})$$

where the membrane potential can be expressed as

$$U_{\text{eq},m} = U'_m + U'_{\text{eq},m} \quad (\text{C.7})$$

with

$$U'_m = \frac{RT}{F} \ln \left(\frac{\gamma_{\text{Cl}^-,+}^b}{\gamma_{\text{Cl}^-, -}^b} \right) \quad \text{and} \quad U'_{\text{eq},m} = \frac{RT}{F} \ln \left(\frac{c_{\text{Cl}^-,+}^b}{c_{\text{Cl}^-, -}^b} \right). \quad (\text{C.8})$$

Finally, the macroscopic electroneutrality conditions

$$c_{\text{red},\pm}^b + 2c_{\text{ox},\pm}^b - c_{\text{Cl}^-, \pm}^b = 0 \quad (\text{C.9})$$

allow expressing $U'_{\text{eq},m}$ in terms of the electro-active bulk ion concentrations as

$$U'_{\text{eq},m} = \frac{RT}{F} \ln \left(\frac{c_{\text{red},+}^b + 2c_{\text{ox},+}^b}{c_{\text{red},-}^b + 2c_{\text{ox},-}^b} \right). \quad (\text{C.10})$$

Appendix D. Alternative formulation of overpotentials

In thermodynamic equilibrium the thermodynamic driving forces vanish and the electrolyte composition at the electrode surface (just outside the electrochemical double layer) and the bulk is homogeneous, so that $a_\alpha^b = a_\alpha^s$. Thus, the equilibrium voltage can be formulated either in terms of the bulk or surface quantities. The choice of the quantities used in the Nernst relation impacts the form of the Butler-Volmer equation, since the predicted total half-cell voltage must be the same, regardless of which reference quantities are used.

The half-cell voltage can be written as

$$U_\pm = U_{\text{eq},\pm}^b + \eta_\pm^b = U_{\text{eq},\pm}^s + \eta_\pm^s, \quad (\text{D.1})$$

where $U_{\text{eq},\pm}^b$ and $U_{\text{eq},\pm}^s$ refer to the equilibria with respect to the bulk and surface quantities. Analogously, the terms η_\pm^b and η_\pm^s denote the total overpotential with respect to bulk and surface quantities, respectively.

In the following we formulate both the Nernst equation and the Butler-Volmer model in terms of the surface quantities and show the equivalence with respect to the overpotential defined in terms of the bulk quantities.

Appendix E. Polarisation with respect to bulk quantities

The equilibrium half-cell potentials can be written in terms of surface quantities as

$$U_{\text{eq},\pm}^s = U_{\text{eq},\pm}^{s,o} + U_{\text{eq},\pm}^{s'}, \quad (\text{E.1})$$

where

$$U_{\text{eq},\pm}^{s'} = -\frac{RT}{F} \ln \left(\frac{c_{\text{red},\pm}^s}{c_{\text{ox},\pm}^s} \right). \quad (\text{E.2})$$

The superscript *s* underlines that the corresponding quantity is evaluated at the electrode surface. To connect the unknown surface species activities to the activities in the bulk of the electrolyte, we proceed similarly to Murthy et al. [16] by expressing the surface quantities in terms of the known bulk quantities using relation (23), which allows writing Eq. (E.1) as

$$U_{\text{eq},\pm}^s = U_{\text{eq},\pm}^{b,s'} + U_{\text{eq},\pm}^{b'} + \eta_{\text{ref},\pm}, \quad (\text{E.3})$$

where

$$\begin{aligned}\eta_{\text{ref},\pm} &= -\frac{RT}{F} \ln \left[\left(\frac{1 - \Delta\gamma_{\text{red},\pm} / \gamma_{\text{red},\pm}^b}{1 - \Delta\gamma_{\text{ox},\pm} / \gamma_{\text{ox},\pm}^b} \right) \left(\frac{1 - \Delta c_{\text{red},\pm} / c_{\text{red},\pm}^b}{1 - \Delta c_{\text{ox},\pm} / c_{\text{ox},\pm}^b} \right) \right] \\ &= -\frac{RT}{F} \ln \left(\frac{g_{\text{red},\pm}^y}{g_{\text{ox},\pm}^y} \right) - \frac{RT}{F} \ln \left(\frac{g_{\text{red},\pm}^c}{g_{\text{ox},\pm}^c} \right) \\ &= -\frac{RT}{F} \ln \left(\frac{g_{\text{red},\pm}^a}{g_{\text{ox},\pm}^a} \right)\end{aligned}\quad (\text{E.4})$$

with

$$g_{a,\pm}^y = \frac{\gamma_{a,\pm}^s}{\gamma_{a,\pm}^b}, \quad g_{a,\pm}^a = \frac{a_{a,\pm}^s}{a_{a,\pm}^b} \quad (\text{E.5})$$

is the polarisation with respect to the reference bulk quantities [26].

Appendix F. Derivation of the Butler-Volmer overpotentials

Let us consider the flow of electrolyte through a porous carbon fiber electrode. The assumption of negligible concentration variations in the electrolyte bulk allows to simplify the transport problem and focus on the transport of species through the boundary layer forming around the carbon fibers. The solution to this transport problem determines the concentrations of the electroactive species at the electrode surface in terms of the electric current and bulk concentrations, which in turn allows the evaluation of the Butler-Volmer overpotential.

The Butler-Volmer equation can be written as in terms of surface quantities as

$$i = i_0^s (e^{(1-\alpha)f\eta^s} - e^{-\alpha f\eta^s}) \quad (\text{F.1})$$

with the exchange current density

$$i_0^s = Fk_0 (c_{\text{ox}}^s)^{1-\alpha} (c_{\text{red}}^s)^\alpha, \quad (\text{F.2})$$

see e.g. Newman and Thomas-Alyea [35] on p. 212.

As in Section 5, we consider the symmetry coefficient to be given by $\alpha = 0.5$, which allows expressing the overpotential η^s in terms of the current density. The surface overpotential is then given in non-dimensional form as

$$\bar{\eta}^s = 2\text{arsinh}\left(\frac{\bar{i}}{2i_0^s}\right) = 2\text{arsinh}\left(\frac{\bar{i}}{2i_0^b \sqrt{g_{\text{ox}}^c g_{\text{red}}^c}}\right), \quad (\text{F.3})$$

where i_0^b denotes the exchange current density in terms of the bulk concentrations.

In the following we show the equivalence of the total cell potential based on formulations with respect to surface and bulk quantities. Inserting relation (E.3) into Eq. (D.1) yields

$$\eta^b = \eta^s + \eta_{\text{ref}}. \quad (\text{F.4})$$

From the dimensionless Butler-Volmer equations formulated in terms of bulk and surface molar concentrations we find

$$\begin{aligned}\bar{\eta}^b - \bar{\eta}^s &= 2\ln\left(\frac{\bar{i} + \sqrt{\bar{i}^2 + 4(\bar{i}_0^b)^2 g_{\text{ox}}^c g_{\text{red}}^c}}{2\bar{i}_0^b g_{\text{red}}^c}\right) - 2\text{arsinh}\left(\frac{\bar{i}}{2\bar{i}_0^b \sqrt{g_{\text{ox}}^c g_{\text{red}}^c}}\right) \\ &= 2\left[\ln\left(\frac{\bar{i} + \sqrt{\bar{i}^2 + 4(\bar{i}_0^b)^2 g_{\text{ox}}^c g_{\text{red}}^c}}{2\bar{i}_0^b g_{\text{red}}^c}\right) - \ln\left(\frac{\bar{i}}{2\bar{i}_0^b \sqrt{g_{\text{ox}}^c g_{\text{red}}^c}} + \sqrt{\frac{\bar{i}^2}{4(\bar{i}_0^b)^2 g_{\text{ox}}^c g_{\text{red}}^c} + 1}\right)\right] \\ &= -\ln\left(\frac{g_{\text{red}}^c}{g_{\text{ox}}^c}\right)\end{aligned}\quad (\text{F.5})$$

where we used $\text{arsinh}(x) = \ln(x + \sqrt{x^2 + 1})$. Thus, for the Butler-Volmer equations expressed with respect to bulk and surface quantities to be equivalent, we require

$$\eta_{\text{ref},\pm} = -\frac{RT}{F} \ln\left(\frac{g_{\text{red}}^c}{g_{\text{ox}}^c}\right), \quad (\text{F.6})$$

a sufficient condition for which is that the activity coefficients are homogeneous, so that $\Delta\gamma_{a,\pm} = 0$, see also [26]. Alternatively, Butler-Volmer expressions formulated in terms of activities yield

$$\bar{\eta}^b - \bar{\eta}^s = -\ln\left(\frac{\delta_{\text{red}}^a}{\delta_{\text{ox}}^a}\right) = \eta_{\text{ref}}. \quad (\text{F.7})$$

Appendix G. Non-negativity of the reactant concentration

For the model to be physically plausible, the reactant concentration must remain non-negative throughout the porous electrode.

Starting from the observation that all species concentrations are non-negative as long as the reactant outflow concentration satisfies $c_{\text{react}}^{\text{out}} \geq 0$ we have to investigate if this outflow concentration can become negative. Mass and charge conservation imply that the magnitude of the electric current $|I|$ and the outflow concentration $c_{\text{react}}^{\text{out}}$ are negatively correlated. Let $|I_{\text{crit}}|$ denote the critical current, for which $c_{\text{react}}^{\text{out}} = 0$, so that for $|I| > |I_{\text{crit}}|$ the outflow concentration becomes negative. Clearly, the critical current can only be reached if the limiting current $|I_{\text{lim}}|$ due to diffusive mass transport limitation is larger than the critical current.

According to our model we have that the critical electric current satisfies

$$|I_{\text{crit}}| = F\dot{V}c_{\text{react}}^{\text{in}}, \quad (\text{G.1})$$

while the limiting electric current can be evaluated as

$$|I_{\text{lim}}| = a_s L_{\text{el}} A_{\text{mem}} c_{\text{react}}^b k_m F < a_s L_{\text{el}} A_{\text{mem}} c_{\text{react}}^{\text{in}} k_m F. \quad (\text{G.2})$$

The limiting current is smaller than the critical current if and only if

$$|I_{\text{lim}}| < |I_{\text{crit}}| \Leftrightarrow a_s L_{\text{el}} A_{\text{mem}} k_m < \dot{V} \Leftrightarrow k_m < \frac{\dot{V}}{a_s L_{\text{el}} A_{\text{mem}}}. \quad (\text{G.3})$$

Evaluating the above relation for the used model parameters shows that indeed $|I_{\text{lim}}| < |I_{\text{crit}}|$, so that the mass transport limitation is reached before the outflow concentration can become zero.

References

- [1] T. Janoschka, N. Martin, M.D. Hager, U.S. Schubert, An aqueous redox-flow battery with high capacity and power: the TEMPTMA/MV system, *Angew. Chem. Int. Ed.* 55 (46) (2016) 14427–14430, <https://doi.org/10.1002/anie.201606472>.
- [2] T. Hagemann, J. Winsberg, M. Grube, I. Nischang, T. Janoschka, N. Martin, M. D. Hager, U.S. Schubert, An aqueous all-organic redox-flow battery employing a (2,2,6,6-tetramethylpiperidin-1-yl)oxyl-containing polymer as catholyte and dimethyl viologen dichloride as anolyte, *J. Power Sources* 378 (2018) 546–554, <https://doi.org/10.1016/j.jpowsour.2017.09.007>.
- [3] J. Winsberg, T. Hagemann, T. Janoschka, M.D. Hager, U.S. Schubert, Redox-flow batteries: from metals to organic redox-active materials, *Angew. Chem. Int. Ed.* 56 (3) (2017) 686–711, <https://doi.org/10.1002/anie.201604925>.
- [4] M.R. Mohamed, H. Ahmad, M.N.A. Seman, S. Razali, M.S. Najib, Electrical circuit model of a vanadium redox flow battery using extended Kalman filter, *J. Power Sources* 239 (2013) 284–293, <https://doi.org/10.1016/j.jpowsour.2013.03.127>.
- [5] Z. Wei, K.J. Tseng, N. Wai, T.M. Lim, M. Skyllas-Kazacos, Adaptive estimation of state of charge and capacity with online identified battery model for vanadium redox flow battery, *J. Power Sources* 332 (2016) 389–398, <https://doi.org/10.1016/j.jpowsour.2016.09.123>.
- [6] B. Xiong, Y. Yang, J. Tang, Y. Li, Z. Wei, Y. Su, Q. Zhang, An enhanced equivalent circuit model of vanadium redox flow battery energy storage systems considering thermal effects, *IEEE Access* 7 (2019) 162297–162308, <https://doi.org/10.1109/ACCESS.2019.2952212>.
- [7] M. Vynnycky, Analysis of a model for the operation of a vanadium redox battery, *Energy* 36 (4) (2011) 2242–2256, <https://doi.org/10.1016/j.energy.2010.03.060>.
- [8] G. Qiu, A.S. Joshi, C. Dennison, K. Knehr, E. Kumbar, Y. Sun, 3-D pore-scale resolved model for coupled species/charge/fluid transport in a vanadium redox flow battery, *Electrochim. Acta* 64 (2012) 46–64, <https://doi.org/10.1016/j.electacta.2011.12.065>.
- [9] A. Shah, M. Watt-Smith, F. Walsh, A dynamic performance model for redox-flow batteries involving soluble species, *Electrochim. Acta* 53 (27) (2008) 8087–8100, <https://doi.org/10.1016/j.electacta.2008.05.067>.
- [10] F.T. Wandschneider, D. Finke, S. Grosjean, P. Fischer, K. Pinkwart, J. Tübke, H. Nirschl, Model of a vanadium redox flow battery with an anion exchange membrane and a Larminie-correction, *J. Power Sources* 272 (2014) 436–447, <https://doi.org/10.1016/j.jpowsour.2014.08.082>.
- [11] S. Won, K. Oh, H. Ju, Numerical analysis of vanadium crossover effects in all-vanadium redox flow batteries, *Electrochim. Acta* 177 (2015) 310–320, <https://doi.org/10.1016/j.electacta.2015.01.166>.
- [12] B. Chakrabarti, E. Kalamaras, A.K. Singh, A. Bertei, J. Rubio-Garcia, V. Yufit, K. M. Tenny, B. Wu, F. Tariq, Y.S. Hajimolana, N. Brandon, J. Low, E.P. Roberts, Y.-M. Chiang, F.R. Brushett, Modelling of redox flow battery electrode processes at a range of length scales: a review, *Sustain. Energy Fuels* (2020), <https://doi.org/10.1039/D0SE00667J>.
- [13] M. Pavelka, F. Wandschneider, P. Mazur, Thermodynamic derivation of open circuit voltage in vanadium redox flow batteries, *J. Power Sources* 293 (2015) 400–408, <https://doi.org/10.1016/j.jpowsour.2015.05.049>.
- [14] N. Hayer, M. Kohns, Thermodynamically rigorous description of the open circuit voltage of redox flow batteries, *J. Electrochem. Soc.* 167 (11) (2020) 110516, <https://doi.org/10.1149/1945-7111/ab9e85>.
- [15] A. Sharma, C. Ling, E. Birgersson, M. Vynnycky, M. Han, Verified reduction of dimensionality for an all-vanadium redox flow battery model, *J. Power Sources* 279 (2015) 345–350, <https://doi.org/10.1016/j.jpowsour.2015.01.019>.
- [16] S.K. Murthy, A.K. Sharma, C. Choo, E. Birgersson, Analysis of concentration overpotential in an all-vanadium redox flow battery, *J. Electrochem. Soc.* 165 (9) (2018) A1746, <https://doi.org/10.1149/2.0681809jes>.
- [17] P.A. Boettcher, E. Agar, C.R. Dennison, E.C. Kumbar, Modeling of ion crossover in vanadium redox flow batteries: a computationally-efficient lumped parameter approach for extended cycling, *J. Electrochem. Soc.* 163 (1) (2016) A5244–A5252, <https://doi.org/10.1149/2.0311601jes>.
- [18] Q. Cacciottolo, M. Petit, D. Pasquier, Fast computing flow battery modeling to optimize the choice of electrolytes and operating conditions – application to aqueous organic electrolytes, *Electrochim. Acta* 392 (2021) 138961, <https://doi.org/10.1016/j.electacta.2021.138961>.
- [19] Q. Xu, T. Zhao, Fundamental models for flow batteries, *Prog. Energy Combust. Sci.* 49 (2015) 40–58, <https://doi.org/10.1016/j.pecs.2015.02.001>.
- [20] L. Ge, L. Bernasconi, P. Hunt, Linking electronic and molecular structure: insight into aqueous chloride solvation, *Phys. Chem. Chem. Phys.* 15 (31) (2013) 13169, <https://doi.org/10.1039/c3cp50652e>.
- [21] A. Heintz, C. Illenberger, Thermodynamics of vanadium redox flow batteries - electrochemical and calorimetric investigations, *Berichte Bunsenges. Für Phys. Chem.* 102 (10) (1998) 1401–1409, <https://doi.org/10.1002/bbpc.199800009>.
- [22] D. del Olmo, M. Pavelka, J. Kosek, Open-circuit voltage comes from non-equilibrium thermodynamics, *J. Non-Equilib. Thermodyn.* 46 (1) (2021) 91–108, <https://doi.org/10.1515/jnet-2020-0070>.
- [23] A.J. Bard, L.R. Faulkner, *Electrochemical Methods: Fundamentals and Applications*, second ed., John Wiley & Sons, 2000.
- [24] D. Kondepudi, I. Prigogine, *Modern Thermodynamics, From Heat Engines to Dissipative Structures*, second ed., Wiley, 2014.
- [25] D. Stephenson, S. Kim, F. Chen, E. Thomsen, V. Viswanathan, W. Wang, V. Sprenkle, Electrochemical model of the Fe/V redox flow battery, *J. Electrochem. Soc.* 159 (12) (2012) A1993–A2000.
- [26] E.J. Dickinson, A.J. Wain, The Butler-Volmer equation in electrochemical theory: origins, value, and practical application, *J. Electroanal. Chem.* 872 (2020) 114145, <https://doi.org/10.1016/j.jelechem.2020.114145>.
- [27] M.S. Kilic, M.Z. Bazant, A. Ajdari, Steric effects in the dynamics of electrolytes at large applied voltages. II. Modified Poisson-Nernst-Planck equations, *Phys. Rev. E* 75 (2) (2007) 021503, <https://doi.org/10.1103/PhysRevE.75.021503>.
- [28] D. Schmal, J. Van Erkel, P.J. Van Duin, Mass transfer at carbon fibre electrodes, *J. Appl. Electrochem.* 16 (3) (1986) 422–430, <https://doi.org/10.1007/BF01008853>.

- [29] X. You, Q. Ye, P. Cheng, The dependence of mass transfer coefficient on the electrolyte velocity in carbon felt electrodes: determination and validation, *J. Electrochem. Soc.* 164 (11) (2017) E3386–E3394, <https://doi.org/10.1149/2.0401711jes>.
- [30] K. Kinoshita, Mass-transfer study of carbon felt, flow-through electrode, *J. Electrochem. Soc.* 129 (9) (1982) 1993, <https://doi.org/10.1149/1.2124338>.
- [31] A.A. Shah, R. Tangirala, R. Singh, R.G.A. Wills, F.C. Walsh, A dynamic unit cell model for the all-vanadium flow battery, *J. Electrochem. Soc.* 158 (6) (2011) A671, <https://doi.org/10.1149/1.3561426>.
- [32] M. Eigen, E. Wicke, The thermodynamics of electrolytes at higher concentration, *J. Phys. Chem.* 58 (9) (1954) 702–714, <https://doi.org/10.1021/j150519a007>.
- [33] M.-C. Yang, E.L. Cussler, Designing hollow-fiber contactors, *AIChE J.* 32 (11) (1986) 1910–1916, <https://doi.org/10.1002/aic.690321117>.
- [34] A.A. Saltelli, *Sensitivity Analysis in Practice: A Guide to Assessing Scientific Models*, Wiley, Chichester, Hoboken, NJ, 2004.
- [35] J. Newman, K.E. Thomas-Alyea, *Electrochemical Systems*, John Wiley & Sons, Hoboken, NJ, USA, 2004.